Research Article | Vol. 34, No. 11 / 1 Jun 2026 / Optics Express 20703
Optics EXPRESS

Soliton glasses in Fabry-Perot resonators

JOSHUA T. YOUNG,[1,2] MATTHEW PUCKETT,[3] LOGAN COURTRIGHT,[1] PRADYOTH H. SHANDILYA,[1] GRACE C. KERBER,[4] STEVEN CUNDIFF,[4] JIANFENG WU,[3] KARL D. NELSON,[5] CHAD HOYT,[5] JONATHAN HU,[2,*] AND CURTIS R. MENYUK[1]

[1]*University of Maryland Baltimore County, Baltimore, MD 21227, USA*
[2]*Baylor University, Waco, TX 76798, USA*
[3]*Honeywell International, Aerospace Advanced Technology Advanced Sensors & Microsystems, Phoenix, AZ 85027, USA*
[4]*University of Michigan, Ann Arbor, Michigan 48109, USA*
[5]*Honeywell International, Plymouth, MN 55441, USA*
[*]*jonathan_hu@baylor.edu*

Abstract: Frequency combs generated in microresonators by nonlinear states, such as soliton crystals, with crystalline defects can provide a rich optical spectrum that is useful for RF applications. In this paper, we report on the existence of a novel soliton glass solution to a modified Lugiato-Lefever equation, which we then show can be theoretically stable for Fabry-Perot microresonators. Soliton glasses are unique compared to previously reported soliton crystals and molecules in that soliton glasses produce a spectral line spacing that equals the inverse of the repetition time of the waveform in the cavity, accompanied by a stable aperiodic temporal spacing between soliton pulses in the resonator. Like a material glass, the soliton glass is characterized by short-range order and long-range disorder. We show that there are transition regions to access the soliton glass that go through spatio-temporal chaos. We computationally verify the stability of the glass over time scales equal to 2000 photon lifetimes using conventional evolutionary simulations in the presence of substantial noise. We also demonstrate the linear stability of the glass solutions by showing that any perturbations decay on a time scale that is on the order of the photon lifetime.

© 2026 Optica Publishing Group under the terms of the Optica Open Access Publishing Agreement

1. Introduction

Optical frequency combs have been the subject of a large amount of interest due to their applications in time generation and transfer [1,2], astronomy [3], and RF generation [4,5], among numerous other applications [6–8]. Most frequency comb solutions that have been theoretically and experimentally demonstrated exhibit some tradeoffs in the usable comb bandwidth, density of comb lines, and relative power between lines. Examples of solutions that have been demonstrated in microresonators include cnoidal waves (Turing rolls and soliton crystals) [9,10], single solitons [11], and soliton molecules [12–14]. Cnoidal waves can provide a wide comb spectrum since the lines are separated by multiples of the free-spectral-range (FSR); however, this large spacing between lines may limit usability in some applications where low FSRs are needed. On the other hand, single solitons and soliton molecules have a period that equals the round-trip time in the cavity, resulting in spectral lines that are spaced by the FSR. All these soliton systems are commonly modelled by a nonlinear Schrödinger equation with the addition of a damping and a driving term [15]. This equation is commonly referred to as the Lugiato-Lefever Equation (LLE) [16–18]. The LLE assumes that the chromatic dispersion is purely quadratic. In practice, it is often necessary to modify the LLE to include the full chromatic dispersion, in which case it is referred to as a modified LLE.

#593425 https://doi.org/10.1364/OE.593425
Journal © 2026 Received 11 Feb 2026; revised 2 May 2026; accepted 4 May 2026; published 28 May 2026

Optics EXPRESS

Soliton crystals [19–22] are another soliton waveform that has attracted much recent attention. Different types of soliton crystal formations have been reported, such as soliton crystals with equally spaced pulses, sometimes referred as perfect soliton crystals [19–21], as well as soliton ensembles with crystal defects, sometimes referred as soliton liquids [21]. Perfect soliton crystals yield an optical spectrum that is similar to Turing rolls, in that the comb lines are spaced apart by several multiples of the FSR. Indeed, there is no consistent distinction between them in the literature, although the term "Turing rolls" has usually been reserved for solutions with large pedestals that typically appear at small frequency detunings of the pump laser from resonance, while the term "soliton crystals" has usually been reserved for solutions with well-defined soliton components that typically appear at large detunings. They have been referred to collectively as cnoidal waves [9,10]. Perfect soliton crystals, like soliton molecules or single solitons, have spectra that contain a smooth envelope [22]. Crystals with defects and the reported soliton liquids result in a rich spectrum separated by a single FSR. Soliton pulses are periodically-spaced in the resonator with the exception of one or more vacancies or one or more extended spacings [21]. In the past, the generation of soliton crystals has been linked to the presence of avoided crossings [19,21]. However, there are still distinct peaks in the spectrum, which have a characteristic "shower-curtain" shape, and the power of many of the lines between the peaks is low, which limits the usefulness of the spectrum in practical applications.

Here, we describe a novel solution to the Lugiato-Lefever equation (LLE), which we call a soliton glass. This solution is characterized by dozens of stable, aperiodically-spaced soliton pulses. Like a glass, this solution is characterized by short-range order, long-range disorder, and is temporally stable [23]. It is characterized by a broad spectrum with a line spacing equal to a single FSR and significant power present throughout the entire spectral bandwidth. This paper extends a prior meeting publication [24]. Here, we verify the stability of the soliton glass solution for the LLE using evolutionary [9,18] and dynamical [9] methods. We show that soliton glasses can be supported in Fabry-Perot resonators fabricated with low anomalous, near-zero dispersion.

In condensed-matter physics, substances are commonly characterized by the presence or absence of long-range and short-range order [23,25]. Systems that exhibit both short-range and long-range order are classified as crystals, even in the presence of defects. When neither short-range nor long-range order is present, the system is a gas. Systems that possess short-range order but lack long-range order are classified as liquids or glasses. The key distinction between a liquid and a glass lies in their dynamics: particles in a liquid continuously rearrange in time, whereas in a glass the particle configuration remains stable in time. An analogous classification applies to photonic soliton states. Soliton crystals exhibit both short-range and long-range order, with pulses arranged periodically around the resonator, while soliton molecules possess only short-range order in the form of tightly bound soliton clusters with fixed internal separations. Finally, multi-soliton states lack both short-range and long-range order [26]. Soliton glasses constitute a distinct regime characterized by short-range order and long-range disorder, while remaining temporally stable. This combination of local order and global disorder results in a dense frequency comb with a single-FSR spacing and substantial power across the full spectral bandwidth.

2. Fabry-Perot resonators and the Lugiato-LeFever equation

Microring resonators that generate a frequency comb with a broad spectrum have been fabricated and used in a number of applications; however, they typically have an FSR that is too large to be directly used in applications that require radio frequency detection [27]. As a result, they are often combined in systems with multiple microring resonators and complex locking electronics [28]. Moreover, tuning the dispersion in a conventional microring is challenging since the material dispersion typically dominates the total dispersion. Hence, we focus on Fabry–Perot resonator structures, in which the dispersion can be precisely engineered by adjusting the chirped

Optics EXPRESS

mirror dimensions. We specifically address a design based on a waveguide resonator with Bragg gratings, realized by sidewall modulation at the two ends of the linear cavity. Figure 1 shows a schematic illustration of a Fabry–Perot resonator incorporating linearly chirped Bragg gratings. Changing the relative length between the gratings on either end will add or remove phase delay between short and long wavelengths. As a result, it is possible to fine-tune the overall dispersion in addition to broadly tuning the dispersion between normal and anomalous, which contributes to the forming of the glass state.

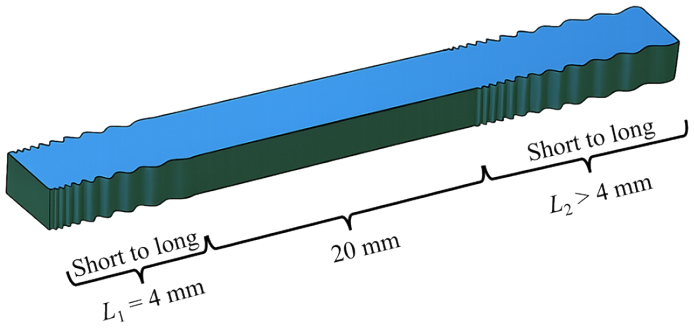

Fig. 1. Schematic illustration of a waveguide Fabry-Perot resonator with chirped Bragg gratings as mirrors. The two blue regions show the chirped Bragg gratings, and the center grey region represents the linear cavity. The overall dispersion is determined by the combined dispersion of all three segments. The relative dimensions shown are not to scale, and the transverse dimension is intentionally magnified to improve visual clarity of the schematic.

As schematically shown in Fig. 1, light reflected from the left side of the Fabry-Perot resonator will experience longer grating periods in the grating before experiencing shorter grating periods. Light interacting with the grating on the right will first experience shorter periods and then longer periods. As a result, different wavelengths will reflect at different longitudinal locations, giving different effective cavity lengths and different net phase delays. For the device to operate in the anomalous dispersion regime, the net phase delay from both segments must more than compensate for normal dispersion in the unchirped portion of the resonator. In the cases that we consider in this paper, the left grating has a length of $L_1 = 4$ mm, the length of the unchirped waveguide region is 20 mm, and the right grating length is longer than the left grating by an amount on the order of several hundred micrometers [29,30]. Due to the longer length of the right grating, longer wavelengths will travel a longer distance than short wavelengths for one roundtrip within the cavity. Through a careful choice of the grating lengths, it is possible to obtain net anomalous dispersion. When this dispersion is equally countered by SPM, solitons generation occurs. A challenge to obtaining stable glass solutions is that the soliton pulses tend to collapse into a small number of pulses—on the order of five or six—when the anomalous dispersion becomes too large. It is thus necessary to carefully control the total dispersion in order to obtain a stable soliton glass. To model the Fabry-Perot resonators, we start with the normalized LLE along with additional modifications [31]

$$\begin{aligned}\frac{\partial\psi(\theta,t)}{\partial t} = &-\sum_m [iD(m)+\kappa(m)]\tilde{\psi}(m,t)\exp(im\theta) + i|\psi(\theta,t)|^2\psi(\theta,t) - i\alpha\psi(\theta,t)\\ &+F + 2i\left\langle|\psi(\theta,t)|^2\right\rangle\psi(\theta,t) - \tau\frac{\partial\psi(\theta,t)}{\partial\theta},\end{aligned} \tag{1}$$

where $\psi(\theta,t)$ is the electric field envelope normalized with respect to the Kerr coefficient, θ is distance normalized to 2π, with the interval $[-\pi,0]$ corresponding to forward propagation in the cavity and the interval $[0,\pi]$ corresponding to backward propagation, t is time normalized to the

Optics EXPRESS

photon lifetime of the central mode, α is the normalized frequency detuning, $\langle|\psi|^2\rangle$ represents the spatial average of $|\psi|^2$, D represents dispersion, and κ represents the mode-number-dependent loss. The normalized amplitude of the input field is F and is proportional to the square root of the input power. In our simulations, we use experimentally measured values for D and κ. We use $\psi(\theta,t)$ and $\tilde{\psi}(m,t)$ to denote the Fourier transform pairs that are related via the relations

$$\tilde{\psi}(m,t) = \int_{-\pi}^{\pi} \psi(\theta,t)\exp(-im\theta)\frac{d\theta}{2\pi}\ ,\ \psi(\theta,t) = \sum\nolimits_m \tilde{\psi}(m,t)\exp(im\theta). \tag{2}$$

When D and/or κ are asymmetric about the central mode number, a drift in the time domain solution will occur, corresponding physically to a change in the group velocity. The computational effect of this drift can be removed systematically with the addition of the final term in Eq. (1), where τ is the normalized drift velocity that we determine numerically. Compared to the conventional LLE, Eq. (1) includes full chromatic dispersion. In addition, we also include the additional term, $2i\langle|\psi|^2\rangle\psi$, to account for the cross-phase modulation [31] that appears because a Fabry-Perot resonator is a linear cavity, so that each pulse interacts with the train of back-reflected pulses. The expression for $\kappa(m)$ is described in Sec. S.1 of the Supplement 1. We used a central wavelength of 1538 nm in our simulations—a common wavelength used for optical communications and for which relatively inexpensive sources exist. This wavelength also corresponds to the pump wavelength and mode number $\mu = 0$.

We assume that the phase change per round trip in the Fabry-Perot device is small and that the dispersion contributions from the gratings and the cavity may be averaged to yield a net dispersion. The round-trip time in the resonator is on the order of picoseconds, which is a few orders of magnitude smaller than the photon lifetime, which is on the order of nanoseconds.

We have studied whether it is possible to obtain glass solutions in microring resonators, in which the cross-phase term that is present in Fabry-Perot resonators does not appear. We only observed small groups of soliton molecules or a single large soliton molecule, but no glasses, as described in Sec. S.2 of the Supplement 1.

3. Characteristics of soliton glasses

In most resonators, detuning the resonant frequency of the system away from its central or intrinsic resonance is done to control the device's spectral response. The balancing of the self-phase modulation and dispersion is what determines the final soliton state, and therefore the device's spectral response. Accessing the soliton glass solutions requires the detuning to be swept through the chaotic region. Figure 2(a) shows the steady-state soliton glass solution as a function of position, normalized to 2π, within the Fabry-Perot resonator cavity. The experimentally measured dispersion from an in-house fabricated device at Honeywell International, Aerospace Advanced Technology Advanced Sensors & Microsystems [29,30] is used in our simulation and is shown in Fig. 2(b). Figure 2(c) shows the detuning sweep over the evolution of 2000 photon lifetimes, corresponding to 56 μs with a photon lifetime around 14 ns. The normalized detuning α, defined in Eq. (1), is swept starting at 0 and asymptotically approaches 16. The normalized input amplitude F equals 4. The normalized time discretization equals 2×10^{-3}. The electric field begins evolving from vacuum noise fluctuations and quantum noise [6], which is included in the simulation and is on the order of 10^{-7} in normalized units. The insets in Fig. 2(c) show different states of the waveform as a function of θ within the resonator at two different detunings. The inset plotted in green corresponds to the green dot on the detuning sweep curve in Fig. 2(c) and shows an initial chaotic state. As the detuning increases, the solution is swept out of resonance for the initial comb, leading to a state of spatiotemporal chaos, as shown in the second inset plotted in red in Fig. 2(c), corresponding to the red dot on the detuning sweep curve. Towards the end of the sweep as detuning increases, a steady glass state is obtained. The blue dot on the sweep curve in Fig. 2(c) corresponds to the final soliton glass waveform, as shown in Fig. 2(a).

Optics EXPRESS

In this case, the steady-state soliton glass solution has 53 pulses. We typically observe 30 to 60 pulses in a soliton glass state. The pump wavelength is offset from the center of the passband of the Fabry-Perot resonator at 1538 nm with the center of the passband at 1545 nm, which we found most easily generates a soliton glass. In Fig. 2(d), we show the power spectrum as a solid blue curve and the passband of the chirped gratings as a dotted red curve. The soliton glass spectrum is above –60 dBc for the majority of the passband and has an asymmetric profile due to the finite passband and the asymmetric dispersion relation. The behavior we observe, in which the initial state is ordered, evolves as a function of detuning into a chaotic state, and finally ends in a state with multiple solitons, resembles the evolution that was observed in the creation of soliton crystals [19,20].

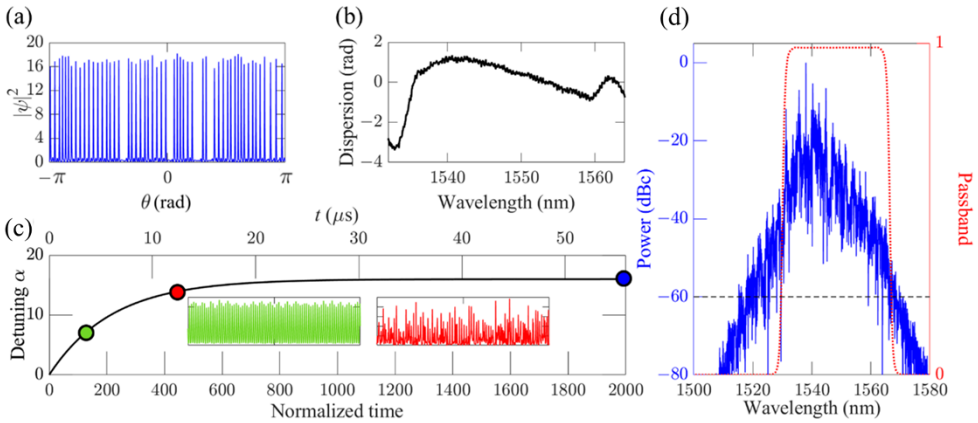

Fig. 2. (a) The computed waveform intensity $|\psi|^2$ as a function of position, normalized to 2π, within the Fabry-Perot resonator at the end of the detuning sweep. (b) Measured dispersion relation for the Fabry-Perot resonator. (c) Illustration of the detuning sweep; the insets show two states of the evolution corresponding to the first two dots. The final blue dot corresponds to the solution in (a). (d) Computed power spectrum and the passband as a function of wavelength.

To determine the temporal stability of the glass solutions, we ran long simulations and carried out a linear stability analysis. For the solution in Fig. 2(a), we ran a simulation of 7×10^4 photon lifetimes, corresponding to about 1 ms, and we saw no change in the glass configuration at the same detuning parameter. The observed stability is consistent with a linear stability analysis that we present in Sec. S.3 of the Supplement 1. We linearly perturb Eq. (1) and determine the eigenvalues and eigenvectors of the linear equation [9]. Aside from a zero eigenvalue that is due to translational invariance, all other eigenvalues have negative real parts close to the photon lifetime, indicating that noise will be rapidly damped.

Next, we study the spatial autocorrelation for the soliton glass. In Fig. 3(a), we show a soliton glass in the spatial domain. The red circles superimposed on the glass solution mark the individual peaks. The individual soliton pulses in the glass state have different peak powers, and nearby pulses have different spacings. In this respect, soliton glasses differ markedly from soliton crystals and soliton molecules. We determine the peaks of individual pulses and their corresponding spatial locations, marked as red circles. We then calculate the spacing as the distance between nearby red circles. The histogram in Fig. 3(b) shows the counts of the distance between nearby red circles. We show a histogram of the individual pulse spacings of the soliton glass solution in Fig. 3(b), which is calculated using the positions of the marked peaks in Fig. 3(a). The most common pulse spacing occurs before $\pi/50$. Figure 3(c) shows the autocorrelation function of the soliton glass, which is calculated while circularly shifting the soliton glass solution

Optics EXPRESS

rather than linearly shifting to account for being in a resonator. The inset in Fig. 3(c) shows an expanded view near zero. The red circle marks the first non-zero peak in the correlation function near 0.013π. The spatial autocorrelation for the soliton glass in Fig. 3(a) resembles the spatial autocorrelation function for condensed-matter glasses [19,20], in that the correlation is high locally but quickly drops off as the shift increases. We only show the correlation function from 0–π since the circular shift will yield a mirror image past π and contains no new information. The red circle in Fig. 3(c) marks the first peak in the autocorrelation function, which coincides with the pulse spacing with the largest count in the histogram. For comparison, the autocorrelation function of soliton molecules exhibits oscillatory behavior with a decaying envelope, while the autocorrelation function of soliton crystals exhibits a purely oscillatory behavior without decay.

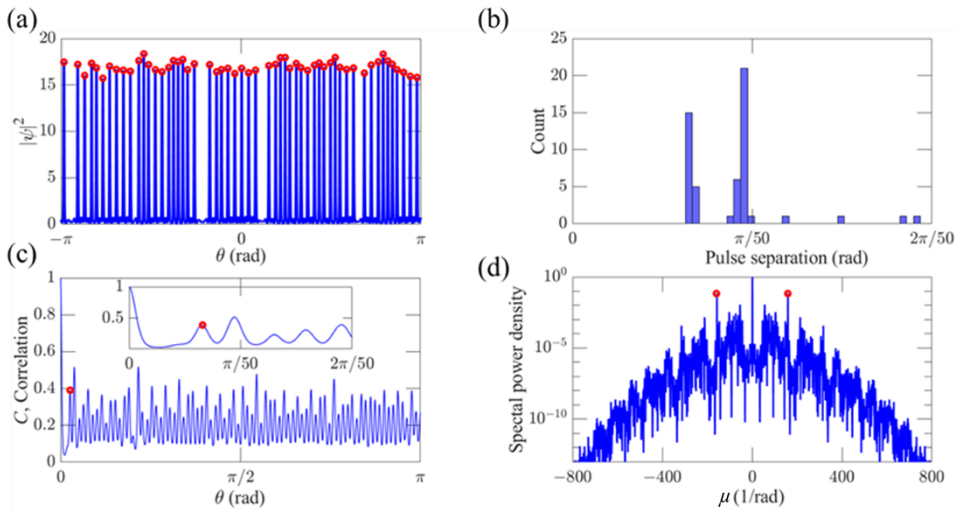

Fig. 3. (a) Soliton glass in the spatial domain. The pulse peaks are marked with red circles. (b) Histogram of the separation between adjacent pulses for the soliton glass in (a). (c) Spatial autocorrelation function and (d) spectral power density for the soliton glass in (a). We show an expanded view of the correlation near zero in the inset of (c). The first peak in the autocorrelation occurs at 0.013π, which matches the highest pulse count in (b). The large peaks in (d) marked with red circles occur at $\kappa = \pm 159$, which is the inverse of the average pulse separation in the soliton glass, $2\pi/159 \approx 0.013\pi$.

Next, we show the spectral power density in Fig. 3(d). Large peaks in the spectral domain occur at $k = \pm$ 159, where k is the spectral domain coordinate. These peaks occur at the inverse of the average pulse separation within the soliton glass $2\pi/159 \approx 0.013\pi$.

4. Repeatability of the soliton glass solution

Next, we study the repeatability of the soliton glass solution as the normalized amplitude (F) and detuning (α) are swept. We show the repeatability contour of the soliton glass solution family in Fig. 4(a). In this α–F space, there are 3 distinct solutions that are supported: chaotic, continuous wave (CW), and soliton glass, which are shown in Fig. 4(a) as red, blue, and white, respectively. The CW state is characterized by constant output. The chaotic state is characterized by a solution with moving pulses and varying amplitude, which are continually changing in time. The glass state is characterized by stable, densely packed, and aperiodically-spaced soliton pulses. We ran 20 different iterations at each combination of α–F so that we could calculate the probability of obtaining a glass solution. The regions that have a solid color correspond to cases where all 20 iterations yielded a particular solution. The upper and lower glass boundaries are plotted

Optics EXPRESS

in a gradient as the space begins to support two different solutions. The chaos-glass boundary is more distinctly defined than is the CW-glass boundary. In the example shown in Fig. 2(c), the final detuning and the normalized input amplitude F are 16 and 4, respectively. These parameters correspond to a glass solution, as shown in Fig. 4(a). We show a few different glass solutions in Fig. 4(b) in the parameter region where glasses can form. While the solutions are not quantitatively the same, they all have similar shapes, minimum spacings, and autocorrelation functions.

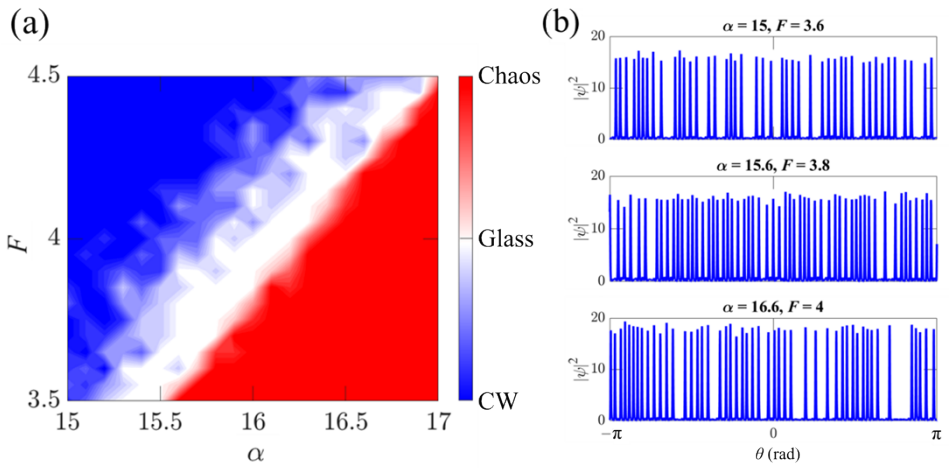

Fig. 4. (a) The α-F contour that yields soliton glasses. Solid red, white, and blue indicate the regions where all the solutions obtained after sweeping are chaotic, soliton glasses, or continuous waves (CW), respectively. Where the colors are mixed, a combination of soliton glasses with either chaotic or CW solutions is obtained. Each point in the contour is averaged over 20 iterations. (b) Examples of soliton glass solutions from the contour in (a).

Next, we study the influence of noise on the soliton glass by adding white noise and using the same input parameters as in Fig. 2 for 2000 photon lifetimes. We increase the noise magnitude until the soliton glass solution is destroyed. Figures 5(a) and 5(c) show the final soliton glass after evolution when just quantum noise is added [9]. Figures 5(b) and 5(d) shows the final soliton glass after evolution when white noise is added. As we increased the white noise amplitude, we found that the soliton glass solution was impervious until the noise magnitude reached 6% of the magnitude of the individual pulses in the glass; larger amounts of white noise resulted in the collapse of the soliton glass to CW or a temporally chaotic state.

5. Conclusions

We described a novel soliton glass solution that consists of densely packed soliton pulses in a Fabry-Perot resonator with slightly anomalous dispersion. We use a measured Fabry-Perot resonator dispersion. Soliton glasses yield a rich, broad spectrum with lines that are separated by a single FSR and nearly all of which have a power greater than −60 dBc across the resonator's stopband. We demonstrated the stability of the glass solutions using both long simulations and a dynamical systems approach, and we found that perturbations should decay on a time scale of a few photon lifetimes, which is several hundred nanoseconds for the examples that we considered. We then studied the stability of the solitons in the presence of quantum and white noise. The soliton glass solution withstood a white noise magnitude of 6% relative to the pulse magnitude in the glass before collapsing.

The glass solution is particularly well suited for RF applications because it enables clean and

Optics EXPRESS

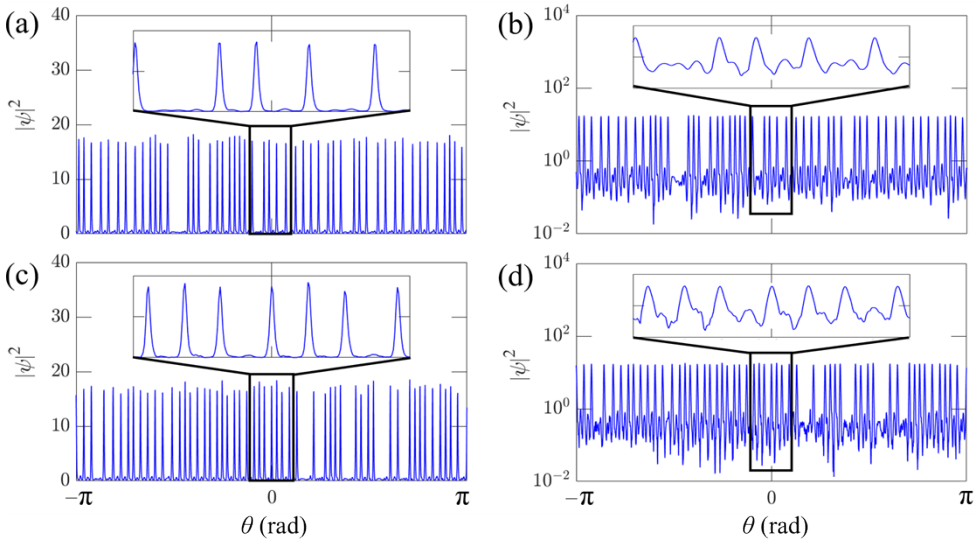

Fig. 5. Soliton glass with a quantum noise level of 1.5×10^{-7} in (a) a linear and (b) a log scale. Soliton glass with a white noise level of 6% relative to the glass magnitude in (c) a linear and (d) a log scale. The black boxes indicate the regions displayed in the zoomed-in plots.

stable microwave generation while avoiding many of the practical limitations of fully ordered soliton states. Upon photodetection of the optical frequency comb, the beating between comb lines can lead to a well-defined RF tone. Hence, the use of soliton glasses is appealing for RF generation and may provide a practical route to obtain stable, broadband, and low-noise RF generation without the need for additional frequency division or complex signal processing.

This paper reports the observation of a soliton glass and demonstrates its stability using both time evolution and dynamical simulations. However, there remains much to be done to fully characterize these novel solutions both theoretically and experimentally. We expect that this initial observation will initiate broader investigations into the roles of dispersion and nonlinearity and facilitate the exploration of potential applications of soliton glass states.

Funding. Air Force Office of Scientific Research (FA9550-20-1-0357, FA8655-25-1-7041); University of Michigan (SUBK00015720).

Disclosures. The authors declare no conflicts of interest.

Data availability. Data underlying the results presented in this paper are not publicly available at this time but may be obtained from the authors upon reasonable request.

Supplemental document. See Supplement 1 for supporting content.

References

1. S. B. Papp, K. Beha, P. Del'Haye, *et al.*, "Microresonator frequency comb optical clock," Optica **1**(1), 10–14 (2014).
2. D. J. Jones, S. A. Diddams, J. K. Ranka, *et al.*, "Carrier-envelope phase control of femtosecond mode-locked lasers and direct optical frequency synthesis," Science **288**(5466), 635–639 (2000).
3. S. A. Diddams, "The evolving optical frequency comb [Invited]," J. Opt. Soc. Am. B **27**(11), B51–B62 (2010).
4. W. Liang, A. A. Savchenkov, V. S. Ilchenko, *et al.*, "Generation of a coherent near-infrared Kerr frequency comb in a monolithic microresonator with normal GVD," Opt. Lett. **39**(10), 2920–2923 (2014).
5. X. Yi, Q.-F. Yang, K. Y. Yang, *et al.*, "Soliton frequency comb at microwave rates in a high-Q silica microresonator," Optica **2**(12), 1078–1085 (2015).
6. T. J. Kippenberg, R. Holzwarth, and S. A. Diddams, "Microresonator-based optical frequency comb," Science **332**(6029), 555–559 (2011).

Optics EXPRESS

7. T. J. Kippenberg, A. L. Gaeta, M. Lipson, *et al.*, "Dissipative Kerr soliton in optical microresonators," Science **361**(6402), eaan8083 (2018).
8. L. A. Lugiato, F. Prati, M. L. Gorodetsky, *et al.*, "From the Lugiato-Lefever equation to Kerr-based optical frequency combs," Phil. Trans. Roy. Soc. A **376**(2135), 20180113 (2018).
9. Z. Qi, S. Wang, J. Jaramillo-Villegas, *et al.*, "Dissipative cnoidal waves (Turing rolls) and the soliton limit in microring resonators," Optica **6**(9), 1220–1232 (2019).
10. A. Coillet, I. Balakireva, R. Henriet, *et al.*, "Azimuthal turing patterns, bright and dark cavity solitons in kerr combs generated with whispering-gallery-mode resonators," IEEE Photonics J. **5**(4), 6100409 (2013).
11. T. Herr, V. Brasch, J. D. Jost, *et al.*, "Temporal solitons in optical microresonators," Nature **8**(2), 145–152 (2014).
12. W. Weng, R. Bouchand, E. Lucas, *et al.*, "Heteronuclear soliton molecules in optical microresonators," Nat. Commun. **11**(1), 2402 (2020).
13. G. Herink, F. Kurtz, B. Jalali, *et al.*, "Real-time spectral interferometry probes the internal dynamics of femtosecond soliton molecules," Science **356**(6333), 50–54 (2017).
14. K. Krupa, K. Nithyanandan, U. Andral, *et al.*, "Real-time observation of internal motion within ultrafast dissipative optical soliton molecules," Phys. Rev. Lett. **118**(24), 243901 (2017).
15. M. Haelterman, S. Trillo, and S. Wabnitz, "Dissipative modulation instability in a nonlinear dispersive ring cavity," Opt. Commun. **91**(5-6), 401–407 (1992).
16. A. B. Matsko, A. A. Savchenkov, W. Liang, *et al.*, "Mode-locked frequency combs," Opt. Lett. **36**(15), 2845–2847 (2011).
17. S. Coen, H. G. Randle, T. Sylvestre, *et al.*, "Modeling of octave-spanning Kerr frequency combs using a generalized mean-field Lugiato–Lefever model," Opt. Lett. **38**(1), 37–39 (2013).
18. Y. K. Chembo and C. R. Menyuk, "Spatiotemporal Lugiato-Lefever formalism for Kerr-comb generation in whispering gallery-mode resonators," Phys. Rev. A **87**(5), 053852 (2013).
19. M. Karpov, M. H. P. Pfeiffer, H. Guo, *et al.*, "Dynamics of soliton crystals in optical microresonators," Nat. Phys. **15**(10), 1071–1077 (2019).
20. W. Wang, Z. Lu, W. Zhang, *et al.*, "Robust soliton crystals in a thermally controlled microresonator," Opt. Lett. **43**(9), 2002–2005 (2018).
21. D. C. Cole, E. S. Lamb, P. Del'Haye, *et al.*, "Soliton crystals in Kerr resonators," Nat. Photonics **11**(10), 671–676 (2017).
22. Z. Lu, H.-J. Chen, W. Wang, *et al.*, "Synthesized soliton crystals," Nat. Commun. **12**(1), 3179 (2021).
23. N. H. Marsh and M. P. Tosi, *Introduction to Liquid State Physics* (World Scientific, 2002), Chap. 10.
24. J. T. Young, M. Puckett, L. Courtright, *et al.*, "Soliton glasses in Fabry-Perot resonators," in *Conference on Lasers and Electro-Optics* (2023), paper FW3B.8.
25. D. L. Goodstein, *States of Matter* (Dover, 1985).
26. N. Pornsuwancharoen, U. Dunmeekaew, and P. P. Yupapin, "Multi-soliton generation using a micro ring resonator system for DWDM based soliton communication," Microw. Opt. Technol. Lett. **51**(5), 1374–1377 (2009).
27. V. J. Urick Jr., J. D. McKinney, and K. J. Williams, *Fundamentals of Microwave Photonics* (Wiley, 2015).
28. D. T. Spencer, T. Drake, T. C. Briles, *et al.*, "An optical frequency synthesizer using integrated photonics," Nature **557**(7703), 81–85 (2018).
29. M. W. Puckett, C. W. Hoyt, J. Wu, *et al.*, "Generating Optical Frequency Combs through Intracavity Phase Compensation," in *Government Microcircuit Applications and Critical Technology Conference* (2023), paper 4.4.
30. G. Kerber, M. Puckett, J. Wu, *et al.*, "Spectral Phase Dispersion Measurements in Frequency Comb Generating Linear Resonators," in *Conference on Lasers and Electro-Optics* (2023), paper JW2A.80.
31. D. C. Cole, A. Gatti, S. B. Papp, *et al.*, "Theory of Kerr frequency combs in Fabry-Perot resonators," Phys. Rev. A **98**(1), 013831 (2018).

Supplemental Document

Optics EXPRESS

Soliton glasses in Fabry-Perot resonators: supplement

JOSHUA T. YOUNG,[1,2] MATTHEW PUCKETT,[3] LOGAN COURTRIGHT,[1] PRADYOTH H. SHANDILYA,[1] GRACE C. KERBER,[4] STEVEN CUNDIFF,[4] JIANFENG WU,[3] KARL D. NELSON,[5] CHAD HOYT,[5] JONATHAN HU,[2,*] AND CURTIS R. MENYUK[1]

[1]*University of Maryland Baltimore County, Baltimore, MD 21227, USA*
[2]*Baylor University, Waco, TX 76798, USA*
[3]*Honeywell International, Aerospace Advanced Technology Advanced Sensors & Microsystems, Phoenix, AZ 85027, USA*
[4]*University of Michigan, Ann Arbor, Michigan 48109, USA*
[5]*Honeywell International, Plymouth, MN 55441, USA*
[*]*jonathan_hu@baylor.edu*

This supplement published with Optica Publishing Group on 28 May 2026 by The Authors under the terms of the Creative Commons Attribution 4.0 License in the format provided by the authors and unedited. Further distribution of this work must maintain attribution to the author(s) and the published article's title, journal citation, and DOI.

Supplement DOI: https://doi.org/10.6084/m9.figshare.32210157

Parent Article DOI: https://doi.org/10.1364/OE.593425

Supplementary Materials

Soliton Glasses in Fabry-Perot Resonators

JOSHUA T. YOUNG,[1,2] MATTHEW PUCKETT,[3] LOGAN COURTRIGHT,[1] PRADYOTH H. SHANDILYA,[1] GRACE C. KERBER,[4] STEVEN CUNDIFF,[4] JIANFENG WU,[3] KARL D. NELSON,[4] CHAD HOYT,[4] JONATHAN HU,[2,*] AND CURTIS R. MENYUK[1]

[1]*University of Maryland Baltimore County, Baltimore, MD 21227, USA*
[2]*Baylor University, Waco, TX 76798, USA*
[3]*Honeywell International, Aerospace Advanced Technology Advanced Sensors & Microsystems, Phoenix, AZ 85027, USA*
[4]*University of Michigan, Ann Arbor, Michigan 48109, USA*
[5]*Honeywell International, Plymouth, MN, 55441, USA*
[*]*Email: jonathan_hu@baylor.edu*

S.1 Frequency-dependent loss based on the transfer matrix method

The loss as a function of the mode number, $\kappa(m)$, that appears in Eq. (1) is defined as

$$\kappa(m) = \left(\frac{1 - R(m)}{N} + l_{\text{ext}}\right) / \left(\frac{1 - R(m_0)}{N} + l_{\text{ext}}\right), \tag{S1}$$

where m is the frequency mode number, R is the loss calculated by the transfer matrix method which is interpolated to the mode number reference to the pump mode number m_0, N is the number of time steps per round trip, and l_{ext} is the linear loss.

S.2 Stability of soliton molecules in conventional micro-ring resonators

In this section we study microring resonators. We use similar parameters to those we used for Fabry-Perot resonators, but with purely parabolic dispersion. While there are soliton molecules that are supported, we did not find any support for soliton glasses as described in the main text. We show in Fig. S1 the simulation results for a conventional microring resonator using the conventional LLE with $\alpha = 9$, $F = 3.4$, and $\beta = -2 \times 10^{-3}$. The pump wavelength is 1540 nm. The normalized dispersion term selected is similar in magnitude to the fitted parabolic dispersion term from the Fabry-Perot dispersion curve. The dispersion for the micro-ring resonators is dominated by the ring waveguide, which does not include a tunable portion like the Fabry-Perot cavity that we described, so the dispersion is usually larger than -2×10^{-3}. We use a smaller dispersion here to show that solutions with multiple aperiodic solitons are possible if we can obtain a small dispersion. However, we have not been able to obtain stable, densely packed solutions that we

consider to be a soliton glass. We determined the stability using time-dependent simulations over milliseconds, and we calculated the dynamical spectrum (eigenvalue spectrum of the linearized equation). We show the result of a typical simulation in Fig. S1, which is generated without the use of a passband. The solution more closely resembles several separate soliton molecules than it does a soliton glass.

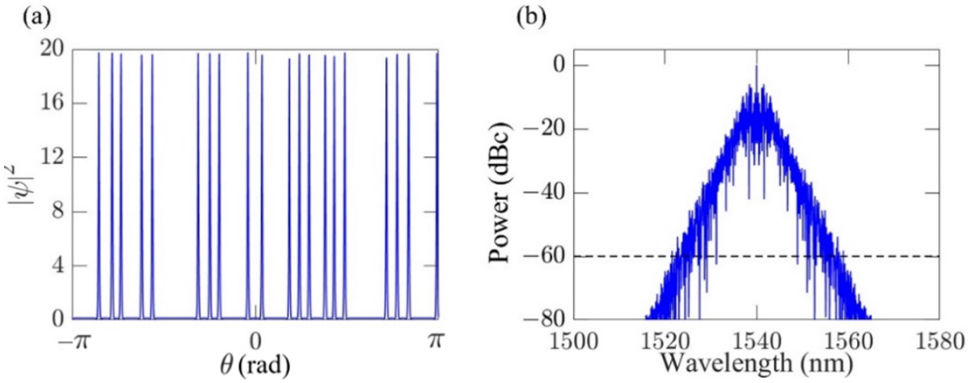

Fig. S1. (a) Intensity $|\psi|^2$ as a function of azimuthal angle within a conventional micro-ring resonator. (b) Power spectrum as a function of wavelength.

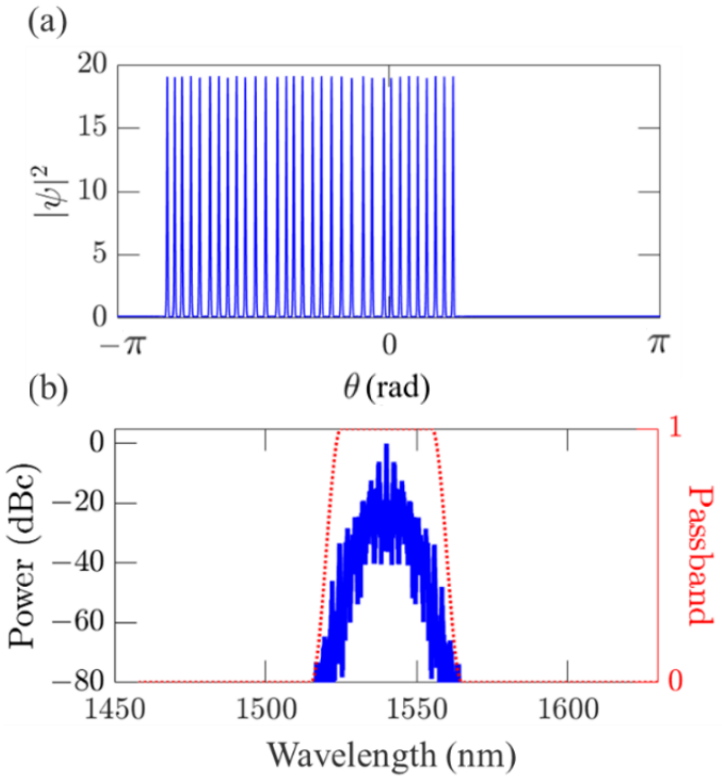

Fig. S2. (a) Soliton molecule with 32 peaks. (b) Spectrum for the soliton molecule and passband as a function of wavelength.

Next, we study the linear stability of imperfect soliton solutions in conventional micro-rings with the addition of a passband that induces a large loss for mode numbers that lie outside the passband. The approach we use is similar to that of Ref. [1]. We fix the normalized power and detuning but reduce the magnitude of the dispersion such that parameter $\beta = -1 \times 10^{-3}$. Figure S2(a) shows the stable soliton molecule with the corresponding spectrum shown in Fig. S2(b). The passband that we use has a full-width half maximum (FWHM) of 40 nm.

The soliton molecule is characterized by 32 aperiodically spaced peaks that are stable in time, followed by a large gap. The relatively narrow 40-nm passband filters out large mode numbers and aids in stabilizing the system. Using equations derived in Sec. S.3 of the supplementary materials, the dynamical spectrum is calculated and shown in Fig. S3.

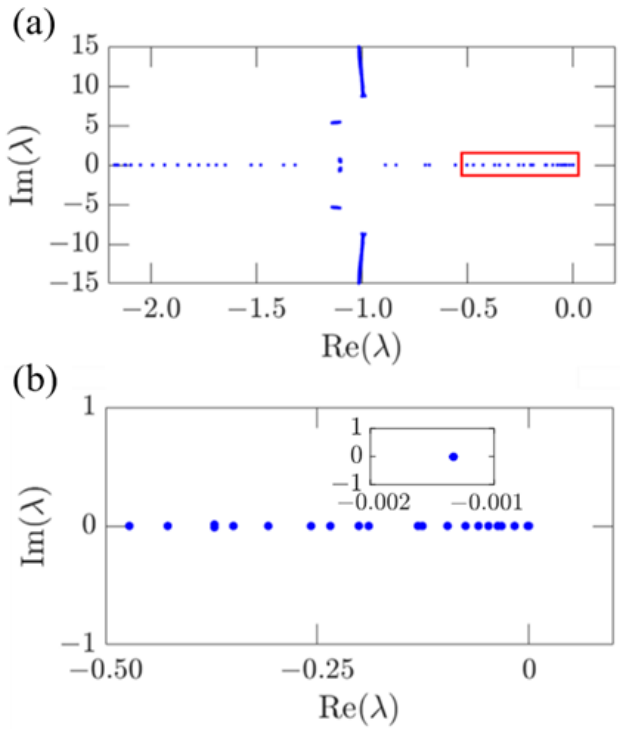

Fig. S3. (a) Dynamical spectrum for the soliton molecule in the microring resonator. The red box marks the region where we show (b) an expanded view of the spectrum near $\lambda = 0$. The inset shows the closest eigenvalue to zero located near -1×10^{-3}.

Figure S3(a) shows the dynamical spectrum for the soliton molecule in Fig. S2(a). There is an eigenvalue located at zero that represents time invariance of the system. Figure S3(b) shows a zoomed in view near 0, which corresponds to the red box in Fig. S3(a), to show the density of eigenvalues next to zero. As the passband broadens to allow more higher mode numbers, the number of eigenvalues that are near zero increases, and they are placed closer to zero. The closest eigenvalue to zero is located near -1×10^{-3} which corresponds to the perturbation most susceptible to noise will decay on the order of 1000 photon lifetimes. Based on a photon lifetime of 14 ns, the closest eigenvalue to zero at -1×10^{-3} indicates a decay time of 1.4 μs. Increasing the passband width pushes eigenvalues to the right of the positive real axis and eventually results in instability. When the passband bandwidth increases, several eigenvalues move to the right, and when the bandwidth is greater than 40 nm, a first eigenvalue crosses the imaginary axis, indicating that the solution has become unstable.

S.3. Linear stability of glasses in the Fabry-Perot resonator

A: Theoretical development

The time evolution analysis provides evidence for stability over the time limit that we ran our simulation, when the results do not diverge. Additionally, we compute the dynamical spectrum of the linearized equation (eigenvalue spectrum) [1] to demonstrate the long-term linear stability of the solution. In this section we derive the Jacobian and minimization equations used in the stability analysis for the Fabry-Perot resonator. First, we start with a modified LLE that includes an added term to account for cross-phase modulation [2] with the $\langle|\psi|^2\rangle$ term representing a spatial average,

$$\frac{\partial\psi(\theta,t)}{\partial t} = -i\sum_m D(m)\tilde{\psi}(m,t)\exp(im\theta) + i|\psi(\theta,t)|^2\psi(\theta,t) - i\alpha\psi(\theta,t) - \sum_m \kappa(m)\tilde{\psi}(m,t)\exp(im\theta) + F + 2i\langle|\psi(\theta,t)|^2\rangle\psi(\theta,t) - \tau\frac{\partial\psi(\theta,t)}{\partial\theta}, \quad \text{(S2)}$$

where D and κ represent dispersion and the mode number-dependent loss. If D and κ are asymmetric, the Fourier transforms will have real and imaginary components that must be considered. Also, if any asymmetry is present there will be a natural drift in the system due to the change in the group velocity that should be removed and which is accounted for by the added $-\tau\frac{\partial\psi}{\partial\theta}$ term. Next, we compose $\tilde{\psi}$ as the sum of its real and imaginary parts using $\tilde{\psi} = \tilde{\psi}_r + i\tilde{\psi}_i$ in the Fourier domain. We then separate Eq. (S2) into its real and imaginary parts, yielding two real equations

$$\mathcal{F}_1 = \frac{\partial\tilde{\psi}_r}{\partial t} = D_r\tilde{\psi}_i + D_i\tilde{\psi}_r - \tilde{\psi}_i\left(\tilde{\psi}_r^2 + \tilde{\psi}_i^2\right) + \alpha\tilde{\psi}_i - K_r\tilde{\psi}_r + K_i\tilde{\psi}_i + F - 2\tilde{\psi}_i\langle\tilde{\psi}_r^2 + \tilde{\psi}_i^2\rangle - \tau D_1\tilde{\psi}_r, \quad \text{(S3)}$$

$$\mathcal{F}_2 = \frac{\partial\tilde{\psi}_i}{\partial t} = -D_r\tilde{\psi}_r + D_i\tilde{\psi}_i + \tilde{\psi}_r\left(\tilde{\psi}_r^2 + \tilde{\psi}_i^2\right) - \alpha\tilde{\psi}_r - K_r\tilde{\psi}_i - K_i\tilde{\psi}_r + 2\tilde{\psi}_r\langle\tilde{\psi}_r^2 + \tilde{\psi}_i^2\rangle - \tau D_1\tilde{\psi}_i, \quad \text{(S4)}$$

where D_r and D_i are the real and imaginary part of the dispersion including loss due to passband. D_1 is the first derivative operator. This gives us the column vector used to minimize as, $\mathcal{F}(\psi_r,\psi_i,\tau) = [\mathcal{F}_1 \quad \mathcal{F}_2]^{\mathrm{T}}$, where the T denotes transpose. Next, we calculate the derivatives for the contributions due to cross-phase modulation:

$$J_{k,l}^{XPM1} = \frac{\partial}{\partial \tilde{\psi}_{r,l}}\left(-2\tilde{\psi}_{i,k}\frac{\Delta\theta}{2\pi}\sum_{m=1}^{N}\tilde{\psi}_{r,m}^2 + \tilde{\psi}_{i,m}^2\right) = -\frac{\Delta\theta}{\pi}\left(2\tilde{\psi}_{i,k}\tilde{\psi}_{r,l}\right), \quad \text{(S5)}$$

$$J_{k,l}^{XPM2} = \frac{\partial}{\partial \tilde{\psi}_{i,l}}\left(-2\tilde{\psi}_{i,k}\frac{\Delta\theta}{2\pi}\sum_{m=1}^{N}\tilde{\psi}_{r,m}^2 + \tilde{\psi}_{i,m}^2\right)$$
$$= -\frac{\Delta\theta}{\pi}\left(2\tilde{\psi}_{i,l}^2 + \delta_{l,k}\sum_{m=1}^{N}\tilde{\psi}_{r,m}^2 + \tilde{\psi}_{i,m}^2\right), \quad \text{(S6)}$$

$$J_{k,l}^{XPM3} = \frac{\partial}{\partial \tilde{\psi}_{r,l}}\left(2\tilde{\psi}_{r,k}\frac{\Delta\theta}{2\pi}\sum_{m=1}^{N}\tilde{\psi}_{r,m}^2 + \tilde{\psi}_{i,m}^2\right)$$
$$= \frac{\Delta\theta}{\pi}\left(2\tilde{\psi}_{r,l}^2 + \delta_{l,k}\sum_{m=1}^{N}\tilde{\psi}_{r,m}^2 + \tilde{\psi}_{i,m}^2\right), \quad \text{(S7)}$$

$$J_{k,l}^{XPM4} = \frac{\partial}{\partial \tilde{\psi}_{i,l}}\left(2\tilde{\psi}_{r,k}\frac{\Delta\theta}{2\pi}\sum_{m=1}^{N}\tilde{\psi}_{r,m}^2 + \tilde{\psi}_{i,m}^2\right) = \frac{\Delta\theta}{\pi}\left(2\tilde{\psi}_{r,k}\tilde{\psi}_{i,l}\right), \quad \text{(S8)}$$

where $\delta_{l,k}$ is the Dirac delta and is 1 when l=k, and 0 otherwise. The accompanying Jacobian that corresponds to $\mathcal{F}$ is calculated by taking the appropriate derivatives of $\mathcal{F}_{1,2}$ with respect to each independent variable in $\mathcal{F}$:

$$\mathcal{J} = \begin{bmatrix} \mathcal{J}_{11} & \mathcal{J}_{12} \\ \mathcal{J}_{21} & \mathcal{J}_{22} \end{bmatrix}, \quad \text{(S9)}$$

where

$$\mathcal{J}_{11} = \frac{\partial \mathcal{F}_1}{\partial \tilde{\psi}_r} = D_i - 2\tilde{\psi}_r\tilde{\psi}_i - \kappa_r - \tau D_1 + J_{k,l}^{XPM1}, \quad \text{(S10)}$$

$$\mathcal{J}_{12} = \frac{\partial \mathcal{F}_1}{\partial \tilde{\psi}_i} = D_r - \tilde{\psi}_r^2 - 3\tilde{\psi}_i^2 + \alpha + \kappa_i + J_{k,l}^{XPM2}, \quad \text{(S11)}$$

$$\mathcal{J}_{21} = \frac{\partial \mathcal{F}_2}{\partial \tilde{\psi}_r} = -D_r + 3\tilde{\psi}_r^2 + \tilde{\psi}_i^2 - \alpha - \kappa_i + J_{k,l}^{XPM3}, \quad \text{(S12)}$$

$$\mathcal{J}_{22} = \frac{\partial \mathcal{F}_2}{\partial \tilde{\psi}_i} = D_i + 2\tilde{\psi}_r\tilde{\psi}_i - \kappa_r - \tau D_1 + J_{k,l}^{XPM4}. \quad \text{(S13)}$$

Using the eigenvalue equation $(\mathcal{J} - I\lambda)\mathcal{F} = 0$, we determine the dynamical spectrum. If any eigenvalues have a positive real part, the system is unstable.

B: Results

We now study the stability of the soliton glass solution in Fig. 2. We use the dynamical method described in the previous section, where we linearize the LLE with the time derivative set to zero. Next, the real and imaginary parts of the LLE are separated. Then an eigenvalue equation that represents the linearized LLE is solved for the eigenvalues and eigenvectors. These eigenvalues quantify the exponential growth or decay that the soliton glass will undergo due to noise or perturbations.

Using the dynamical approach that we describe in Sec. S.3A of the supplementary materials, we calculate the dynamical spectrum for the soliton glass shown in Fig. 2(a). The real part of the eigenvalues of the dynamical spectrum determines the stability of the solution. If all the real parts of the eigenvalues are negative, which implies that all perturbations are suppressed, then the solution is stable. In Fig. S4(a), we plot the dynamical spectrum of the soliton glass in Fig. 2(a). Figure S4(b) features an expanded view of Fig. S4(a) in the neighborhood of zero. There is a singular pole located at zero, which is due to the azimuthal translation symmetry of Eq. (1). Any solution of Eq. (1) remains a solution when translated by a constant amount in θ. The eigenvector for the 0 eigenvalue corresponds to the azimuthal derivative of the soliton glass waveform in Fig. 2(a). The eigenvectors for the other eigenvalues correspond to perturbations that jitter the pulse locations or their phases. The closest non-zero poles form a complex conjugate pair with $\mathrm{Re}(\lambda) = -4.3 \times 10^{-1}$. Any perturbations to the system decays on the scale of two photon lifetimes, which is 32 nanoseconds for the parameters that we chose. Using the same normalized detuning and power of 16 and 4, respectively, we ran 50 different realizations of soliton glasses with different random seeds, the eigenvalues closest to zero are in the range of -10^{-2} to -10^{-1}.

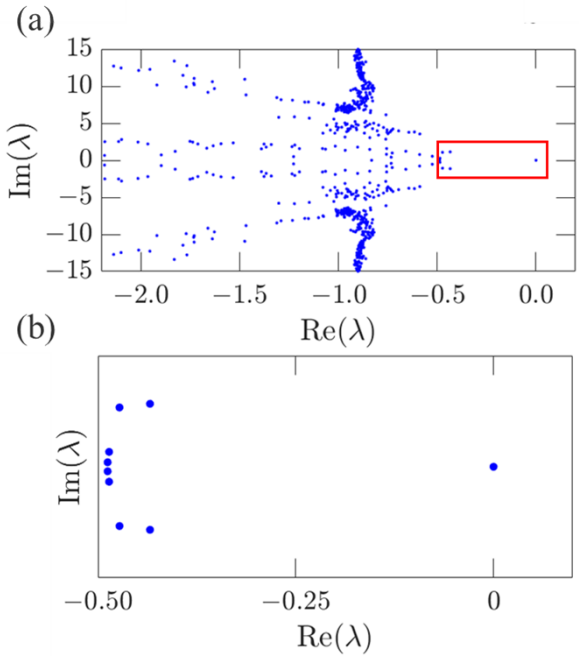

Fig. S4. (a) Dynamical spectrum for the soliton glass that we show in Fig. 3. The red box marks the boundary for (b) the expanded view of the dynamical spectrum close to zero.

The solution of the resonator may consist of a combination of several solutions. Hence, it's important to see the impact of the perturbation to the solution. Next, we study how the soliton glasses react when perturbed by the eigenvector with the closest non-zero eigenvalue to the positive real axis. The blue curve and red curve in Figs. S5(a)–(d) represent the absolute value squared for the soliton glass, and the perturbed soliton glass, respectively. The solid black curves in the upper plots of inserts in Fig. S5(b)–(d) show the difference between the soliton glass and the glass perturbed by the eigenvector. The inset Fig. S5(b) zooms into the gap on the left side of the soliton glass. Adding the perturbation shows that both pulses in the window are moving towards each other to fill in the gap. Figure S5(c) zooms towards the center of the resonator. The perturbation has little effect on the central pulses slightly moving all pulses to the left, even with the right-side pulse in Fig. S5(c) lying on a gap. The inset Fig. S5(d) shows the zoomed in view at a gap towards the right of the resonator. The left pulse moves towards the gap when perturbed whereas the right pulse stays in place. Rather than uniformly closing all gaps such that the pulses are equally spaced, the eigenvector perturbation appears to nudge the soliton glass towards a soliton crystal with crystalline defects.

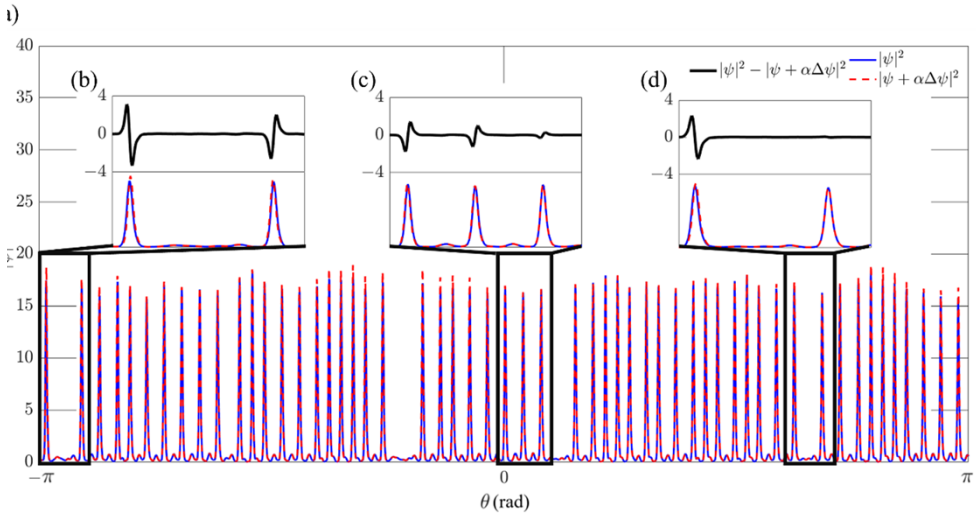

Fig. S5. (a) Soliton glass perturbation comparison as a function of space, (b) zoomed-in plot of the left-side gap, (c) zoomed-in plot near zero, and (d) zoomed-in plot of the right-side gap.

References:

1. Z. Qi, S. Wang, J. Jaramillo-Villegas, M. Qi, A. M. Weiner, G. D'Aguanno, T. F. Carruthers, and C. R. Menyuk, "Dissipative cnoidal waves (Turing rolls) and the soliton limit in microring resonators," Optica **6**(9), 1220–1232 (2019).
2. D. C. Cole, A. Gatti, S. B. Papp, and L. Lugiato, "Theory of Kerr frequency combs in Fabry-Perot resonators," Phys. Rev. A. **98**, 013831 (2018).